8A.7

DEVELOPMENT OF A MULTISCALE MODELING FRAMEWORK FOR URBAN SIMULATIONS IN THE WEATHER RESEARCH AND FORECASTING MODEL

David J. Wiersema*[1,2], Katherine A. Lundquist[1], and Fotini Katopodes Chow[2]

[1]Lawrence Livermore National Laboratory, Computational Engineering Division
[2]University of California Berkeley, Civil and Environmental Engineering

1 INTRODUCTION

Current generation numerical weather prediction (NWP) codes have been extensively developed and validated for mesoscale simulation with horizontal grid resolutions of tens of kilometers. Researchers and forecasters are utilizing advances in computational resources to simulate the planetary boundary layer (PBL) at resolutions beyond the original design space of available NWP codes. Downscaling mesoscale information and simulating the PBL at microscale resolutions is an extremely complex challenge filled with numerous difficulties that have only recently begun to be addressed by the NWP research community.

This paper outlines the development of the Weather Research and Forecasting (WRF) model, a NWP model typically used at the mesoscale, for multiscale simulations over complex terrain. We have implemented a robust and flexible framework that enables downscaling via grid nesting of information from mesoscale domains to microscale domains. Vertical griding of the microscale domains is controlled using the vertical grid refinement method implemented by Daniels et al. (2016), providing control over each grid's aspect ratio ($\frac{\Delta x}{\Delta z}$). A new immersed boundary method (IBM) algorithm, the velocity reconstruction method (VRM), enforces a log-law boundary condition over complex microscale terrain, such as buildings. VRM enables nesting of a microscale IBM domain within a mesoscale terrain-following parent domain, a functionality that was not possible with the previous IBM algorithm, the ghost point method (GPM) (Lundquist et al., 2010, 2012). These additions to the WRF model enable simulations that capture effects across a wider range of scales than previously possible. A single simulation may now contain nested domains with grid resolutions ranging between the mesoscale (kilometers) to the microscale (meters).

To validate the multiscale modeling framework, we have simulated a passive tracer release from the third intensive observational period of the 2003 Joint Urban (JU2003) field campaign in Oklahoma City, OK. A multiscale simulation of this tracer release is compared to two idealized simulations, using GPM and VRM. The idealized simulations are configured similar to previous modeling efforts by Lundquist et al. (2012) and use a two-domain nested setup with grid resolutions of 10 m and 2 m, periodic lateral boundary conditions on the outer domain, and a pressure gradient forcing derived from JU2003 observations. In comparison, the multiscale simulation has five nested domains with resolutions ranging from 6.05 km to 2 m. The simulation is initialized and forced using only data from the NCEP North American Regional Reanalysis. Predictions of velocities and passive tracer concentration from the three simulations are compared to the JU2003 observations using several statistical measures of model skill.

2 THE IMMERSED BOUNDARY METHOD IN WRF

Microscale simulations over complex terrain have recently become possible in the WRF model with the addition of an immersed boundary method (Lundquist et al., 2010, 2012; Arthur et al., 2016, 2018; Bao et al., 2016, 2018). The modified model, referred to as WRF-IBM, has previously been used for idealized microscale simulations over mountainous and urban terrain. The first use of an IBM was for the simulation of blood flow

*Corresponding author address: 205 O'Brien Hall, Univ. of California Berkeley, Berkeley, CA 94720-1710; email: wiersema@berkeley.edu

through the heart (Peskin, 1972), and since then has been used in many applications. IBM is especially useful for simulation of flow over complex shapes or flexible boundaries because the method does not require complicated meshing and it provides a convenient way to determine forces exerted by fluid on boundaries.

WRF-IBM has a non-conforming structured grid that is independent of the immersed boundary (IB). An example of a vertical slice through a grid located in an urban environment is shown later in Figure 3, with the immersed boundary shown in red. Boundary conditions are imposed at the IB through the addition of a body force term in the conservation equations for momentum and scalars, equations 1 and 2.

$$\partial_t V + V \cdot \nabla V = -\alpha \nabla p + \nu \nabla^2 V + g + F_B \quad (1)$$

$$\partial_t \phi + V \cdot \nabla \phi = \nu_t \nabla^2 \phi + F_\phi + F_B \quad (2)$$

Here V is the velocity vector, ϕ a scalar quantity, α the specific volume, F_B the body force term, and F_ϕ is the additional scalar forcing (Lundquist, 2010; Lundquist et al., 2010, 2012). The F_B and F_ϕ modify the governing equations near the IB and assume values of zero away from the IB. Several variants of the IBM have been implemented into WRF-IBM, however only the ghost point method (GPM) and the velocity reconstruction method (VRM) will be evaluated here. Previous research by Bao et al. (2016, 2018) provides a comparison of several IBM algorithms in the WRF model, including the two methods used here.

2.1 Ghost Point Method

The GPM enforces the desired boundary conditions by applying additional forcing at the computational nodes beneath and adjacent to the IB. These nodes where additional forcing is applied are referred to as "ghost points". To set a ghost point, the location of the point is reflected across the immersed boundary, creating an "image point". The image point's magnitude is calculated using an inverse distance weighting interpolation scheme described in Section 2.3. The ghost point's value is then determined using Equation 3 for a Dirichlet boundary condition or Equation 4 for a Neumann boundary condition.

$$\phi_G = 2\phi_\Omega - \phi_I \quad (3)$$

$$\phi_G = \phi_I - \overline{GI} \frac{\partial \phi}{\partial n}|_\Omega \quad (4)$$

where ϕ_G is the ghost point's value, ϕ_I is the image point's value, and ϕ_Ω is the value at the IB. $\overline{GI}$ is the distance between the ghost and image points and $\frac{\partial \phi}{\partial n}|_\Omega$ is the surface-normal gradient value assigned at the IB for a Neumann boundary condition. WRF-IBM-GPM enforces a no-slip boundary condition for velocity and a no-flux boundary condition for scalars.

Because the GPM requires ghost points beneath the IB, the grid's bottom level is lowered relative to a typical WRF terrain-following grid. This mismatch complicates nesting between terrain-following and GPM domains because continuity of domain height is required across the nest interface. Another problem is discontinuity between a parent domain with WRF's standard log-law boundary condition and a nested GPM domain with a no-slip boundary condition. For these reasons, we have developed a new IBM algorithm, described below, which is more suited to our needs for multiscale modeling because it does not require ghost points and it enforces a log-law that is more consistent with the traditional WRF bottom boundary condition.

2.2 Velocity Reconstruction Method

The velocity reconstruction method (VRM) enforces a log-law, Equation 5, by applying forcing at "reconstruction points", the computational nodes above and adjacent to the IB. The magnitude of each reconstruction point (RP) is determined by finding a vector that is normal to the nearest section of the immersed boundary and passes through the RP. The interpolation point (IP) corresponding to an RP is found as the first intersection of the normal vector with a cell face. The u, v, and w velocities at the IP are determined using an inverse distance weighting interpolation scheme, described in Section 2.3. The coordinate orientation is then rotated to be surface normal to the immersed boundary. Surface normal velocities at the RP are calculated using equations 6, 7, and 8. Finally, the velocities are rotated from the surface normal coordinate orientation back to the native model orientation.

$$u = \frac{u_*}{k} \ln\left(\frac{z}{z_0}\right) \quad (5)$$

$$u_{RP} = u_{IP} \frac{\ln\left(\frac{d_{RP}}{z_0}\right)}{\ln\left(\frac{d_{IP}}{z_0}\right)} \quad (6)$$

$$v_{RP} = v_{IP} \frac{\ln\left(\frac{d_{RP}}{z_0}\right)}{\ln\left(\frac{d_{IP}}{z_0}\right)} \quad (7)$$

$$w_{RP} = w_{IP} \frac{d_{RP}}{d_{IP}} \quad (8)$$

where z_0 is the roughness length, d_{RP} is the distance from the immersed boundary to the reconstruction point, and d_{IP} is the distance from the immersed boundary to the interpolation point. These equations

assume that both the RP and IP are located within the log layer and that the friction velocity (u_*) is constant between the RP and IP.

2.3 Inverse Distance Weighting (IDW) interpolation scheme

The IDW interpolation scheme is used to determine values for image and interpolation points when using GPM and VRM, respectively. First, the nearest neighboring grid points to the image/interpolation point are found. Nearest neighbors are determined by searching a box of grid points, typically sized $4 \times 4 \times 4$, centered on the image/interpolation point. Each point in this box is ranked based upon distance from the image/interpolation point. Points beneath the IB are removed from consideration. For the VRM, reconstruction points are also removed from consideration. The nearest n points are used as the nearest neighbors to the image/interpolation point, where n is 8 for the GPM and 7 for the VRM.

Weights for the nearest neighbors are calculated using Equation 9 where r_{max} is the maximum distance between a nearest neighbor and the image/interpolation point and W is the weight of a nearest neighbor a distance r from the image/interpolation point.

$$W = \left(\frac{r_{max} - r}{r_{max} r} \right)^{\frac{1}{2}} \tag{9}$$

3 VERTICAL GRID REFINEMENT

A key feature required for multiscale simulations is vertical refinement of nested domains. Prior to WRF version 3.8.1, the only available method of vertical grid refinement was `ndown`, a separate program that ingests parent grid output files and generates boundary updates for a nest. Because `ndown` processes output files, the parent simulation must be run to completion before the nested simulation can be run. Additionally, the boundary update frequency is limited to that of the parent grid output, which can prohibit downscaling of resolved turbulent flows.

We previously developed an improved vertical grid refinement method that has been included within the WRF public release since version 3.8.1 (Daniels et al., 2016). This capability allows for domains with different vertical grids to be concurrently nested without requiring a separate program like `ndown`. The lateral boundary conditions of a nest are updated after every time step of the corresponding parent, which removes the need to store large history files for frequent boundary updates. We have also included the ability to specify unique vertical grid levels for every domain in a sequence of nested grids. Additional details regarding the capabilities, implementation, and validation of the vertical nesting framework can be found in Daniels et al. (2016).

The vertical grid refinement capability is a critical component of the multiscale modeling framework described here. The ability to refine vertically provides control over each domain's grid aspect ratio ($\frac{\Delta x}{\Delta z}$), an important variable for accurate large eddy simulations (Mirocha et al., 2013). It should be noted that our multiscale simulation, detailed in Section 6, successfully applies the vertical grid refinement method to a sequence of five nested grids, a considerably more complex configuration than simulations from Daniels et al. (2016).

4 JOINT URBAN 2003 ATMOSPHERIC DISPERSION STUDY

During July of 2003, the Defense Threat Reduction Agency (DTRA) and the U.S. Department of Homeland Security (DHS) worked together to facilitate the Joint Urban 2003 atmospheric dispersion study in Oklahoma City, Oklahoma. Investigators from universities, government laboratories, and private industry participated in the field campaign and analysis. Some of the primary objectives of this field campaign included the investigation of flows downwind of tall buildings and in street canyons and the investigation of tracer dispersion around and downwind of tall buildings. More details can be found in the study overview (Allwine and Flaherty, 2006).

Joint Urban 2003 consisted of ten intensive observational periods (IOPs) of 8-hours throughout the 34-day span of the field campaign. A tracer gas, sulfur hexafluoride (SF_6), was released during each IOP as either a puff or continuous release. Concentrations of the tracer were measured at sites throughout the central business district. The simulations and analysis presented in this paper are limited to the first continuous tracer release of IOP 3 on July 7 2003 from 16:00 to 16:30 UTC. This particular tracer release was selected for analysis because the wind direction was consistent over the 30 minute release period, the atmospheric stability was near-neutral, and there are previous modeling studies to which we can compare. During IOP 3 the SF_6 release location was at the north-east corner of the botanical gardens at 2 m above ground level (AGL) at UTM coordinates (634603, 3925763), marked by the yellow star in Figure 1.

Several JU2003 datasets from IOP 3 have been used for configuration and analysis of simulations including a

miniSODAR deployed by Argonne National Laboratory (ANL), 6 Dugway Proving Grounds (DPG) Portable Weather Information Display Systems (PWIDS) with prop-vane anemometers, 14 DPG super PWIDS with sonic anemometers, and 19 Lawrence Livermore National Laboratory (LLNL) "bluebox" integrated SF_6 measurement stations. The locations of these instruments are displayed in Figure 1.

4.1 Urban geometry

Urban geometry represented by the immersed boundary was set by sampling, at each grid point, a shapefile containing vectorized building information. Narrow gaps between buildings and other insufficiently resolved features were manually adjusted to ensure that each of the IBM-VRM interpolation points had a minimum of two nearest neighbors for the inverse distance weighting interpolation. The elevated walkway at coordinates (634850, 3925800) was omitted from the model topography. Additionally, several buildings near inflow boundaries, specifically the southern edge, were removed due to spurious interactions with the inflow conditions. Identical building geometry was used for both the idealized and multiscale simulations.

Variations in the ground elevation within the microscale modeling domain are small in magnitude, with minimum and maximum elevations of 360 and 365 meters. Due to restrictions from periodic boundary conditions, the idealized simulations ignore the underlying ground topography and only building heights above ground level are included in the immersed boundary height. An advantage of the multiscale simulation, in contrast, is that no periodic boundary conditions are used and the underlying ground topography can be included. For the multiscale simulation, the building heights above ground level are combined with the underlying ground topography interpolated from the parent domain. To maintain flat rooftops, the IB height is averaged at points within each building footprint, which results in minor adjustments within each building geometry.

5 IDEALIZED SIMULATIONS

Previous JU2003 microscale modeling efforts used idealized model configurations with simplified boundary conditions. Chan and Leach (2007), Chow et al. (2008), and Neophytou et al. (2011) all set inflow boundary conditions using steady velocity profiles constructed by fitting a log law profile to SODAR and weather station observations. The idealized simulations presented here adopt a similar configuration to previous WRF-IBM-GPM simulations by Lundquist et al. (2012) that use a two-domain nested configuration to produce turbulent inflow for the nested domain. The parent domain has periodic boundary conditions and a pressure gradient forcing term is adjusted to create agreement between the simulated and observed time averaged velocity profiles.

The observed velocity profile used for our idealized WRF-IBM simulations is the combination of data from a miniSODAR deployed by Argonne National Laboratory (ANL), two Dugway Proving Ground (DPG) PWIDS (stations 10 and 11), two DPG super PWIDS (stations 17 and 20), and the NOAA Air Resources Laboratory Field Research Division (ARLFRD) sonic anemometer located at the SF_6 release location. The ANL miniSODAR data from the 30 minute SF_6 release window was temporally averaged to provide velocities at 5 m increments from 15 to 135 m AGL, shown in Figure 6. Each DPG PWIDS and DPG super PWIDS was temporally averaged over the SF_6 release window. An average of the four stations, with each station given equal weight, was used to estimate velocities at 8 m AGL. Additionally, a ARLFRD sonic anemometer collocated with the SF_6 release site was temporally averaged to provide velocities at 2 m AGL. A combination of these values yields the velocity profile listed in table-3.

Our idealized WRF-IBM simulations use a two-domain setup with a periodic parent domain (D1) at $\Delta x = \Delta y = 10$ m and a nested domain (D2) at $\Delta x = \Delta y = 2$ m. D1 and D2 use time steps of 0.05 and 0.01 s respectively. In the east-west, north-south, and bottom-top dimensions, D1 has dimensions 241 $\times$ 241 $\times$ 146 grid points and D2 has dimensions 351 $\times$ 401 $\times$ 243 grid points. D1 has flat terrain while D2 includes building geometries. Both domains use a Smagorinsky turbulence closure with coefficient $C_s = 0.18$. D1 was run for seven hours to develop statistically steady turbulence prior to initialization of D2. Vertical grid refinement was used to maintain a near surface grid aspect ratio $\frac{\Delta x}{\Delta z} = 2.0$ for each domain. Aloft, the vertical grid levels are spaced increasingly far apart with a constant stretching coefficient, $\frac{z_{k+1}-z_k}{z_k-z_{k-1}}$, of 1.6% for D1 and 2.8% for D2. Upon reaching $\frac{\Delta x}{\Delta z} = 0.5$ the grid aspect ratio is maintained for the remaining vertical grid levels. Due to the need for ghost points beneath each point of the immersed boundary, the WRF-IBM-GPM simulations have two additional levels located approximately 2 m and 4 m beneath the ground level.

The idealized GPM and VRM simulations are forced by the addition of a pressure gradient to the flow. This pressure gradient is adjusted to match the time averaged velocity profile from D2 with the time averaged miniSODAR observations at approximately 40 m AGL,

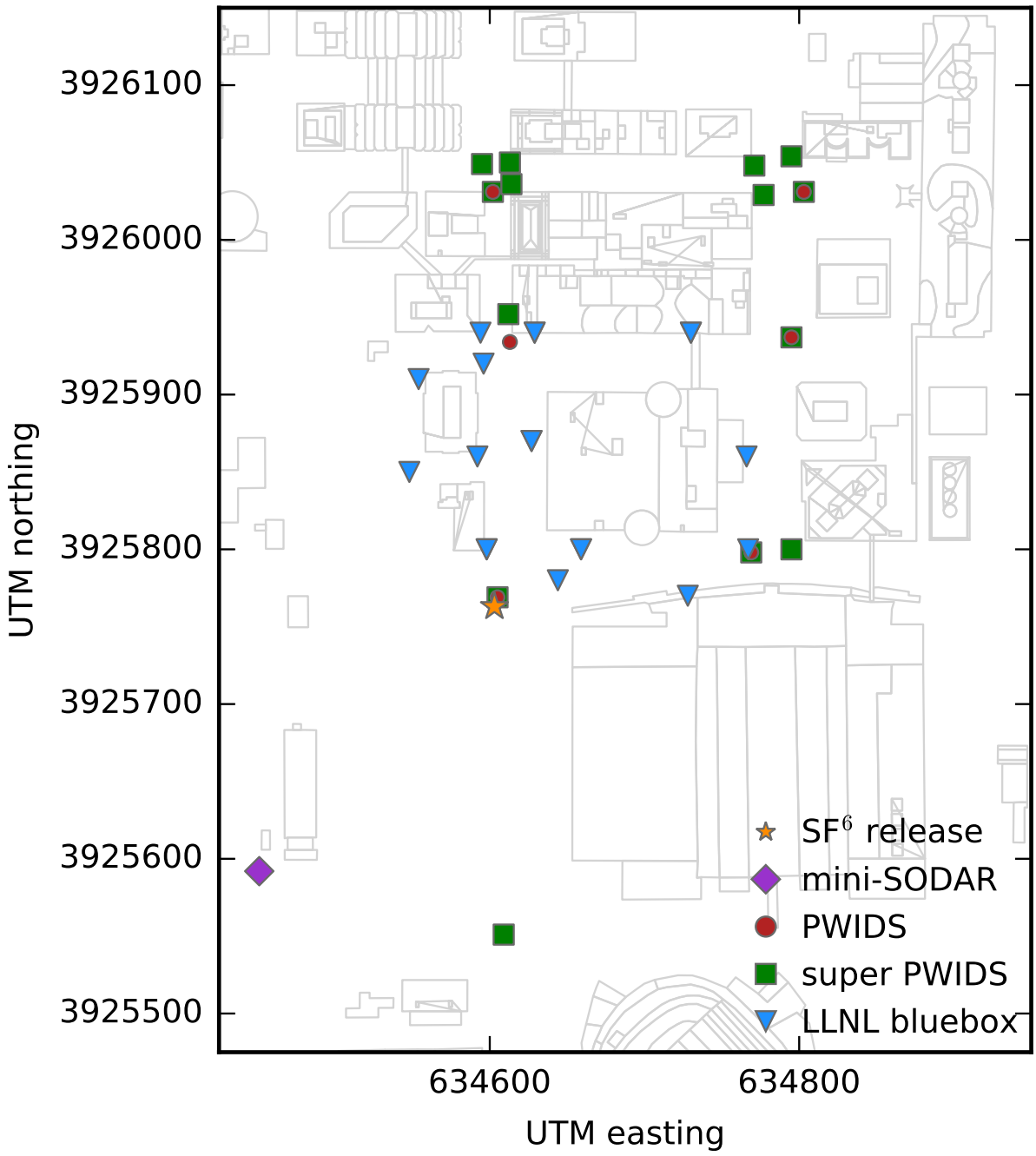

Figure 1: Map of the Oklahoma City business district showing measurement stations used for analysis of simulation results. Siting information for DPG PWIDS and LLNL bluebox stations is contained in tables 1 and 2, respectively. The ANL miniSODAR and SF_6 release location were located at UTM coordinates (634451, 3925592) and (634603, 3925763), respectively.

shown in Figure 6. Both domains have a model top at 400 m AGL and a Rayleigh relaxation layer applied to W-velocities in the topmost 40 m with damping coefficient 0.2.

The GPM simulations used a no-slip bottom boundary condition for velocities and a no-flux condition for scalar variables. The VRM simulations used the log-law boundary condition described in Section 2.2 with

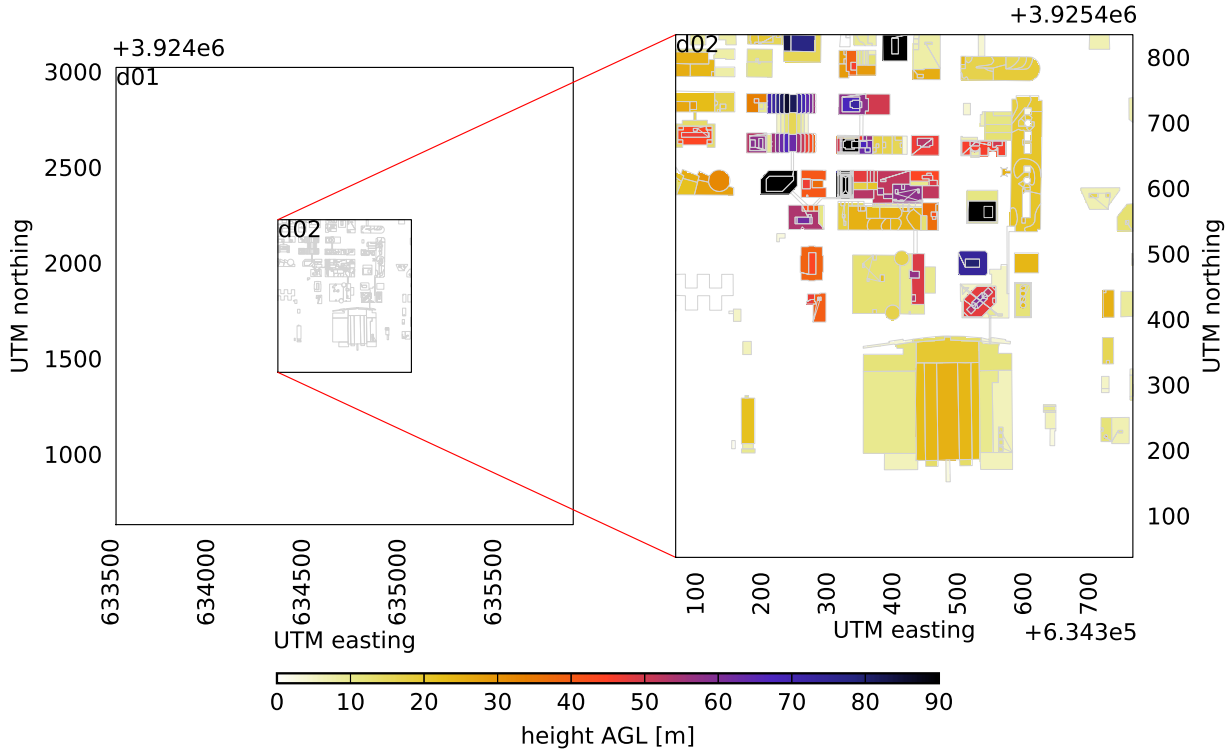

Figure 2: Grid setup used for idealized VRM and GPM simulations. The parent domain is flat with periodic boundary conditions and horizontal dimensions of 241 by 241 grid points with a resolution of 10 m. The nested domain contains buildings resolved with IBM, and has horizontal dimensions of 351 by 401 grid points with a resolution of 2 m.

roughness length z_0=0.1 m and the traditional WRF boundary condition for scalars. A scalar immersed boundary condition that does not require ghost points is currently under development for use with VRM.

6 MULTISCALE SIMULATIONS

The multiscale WRF-IBM simulations use five nested domains with horizontal resolutions of 6.05 km, 550 m, 50 m, 10 m and 2 m. The outermost domain's lateral boundary conditions and initial conditions are prescribed using data from the NCEP North American Regional Reanalysis (Mesinger et al., 2006), which has horizontal resolution of 32 km. The standard WRF terrain-following coordinate is used for the 6.05 km, 550 m, and 50 m domains. WRF-IBM-VRM is enabled for the 10 m and 2 m domains with a constant roughness length $z_0 = 0.1$ m. The 6.05 km and 550 m domains use the MYJ planetary boundary layer scheme while the 50 m, 10 m and 2 m domains use the Smagorinsky turbulence closure scheme with $C_s = 0.18$. A summary of grid configuration and physics options is included in table-4 of the appendix.

The horizontal dimensions of the 10 m and 2 m domains are identical to the dimensions of the corresponding domains in the idealized simulations. A model top of 200 hPa is used for all domains of the multiscale simulation. The 10 m and 2 m grids thus extend significantly higher than the comparable grids from the idealized simulations. Near surface vertical grid levels for the 10 m and 2 m domains are selected to match as closely as possible those used in the comparable domains of the idealized VRM simulation. Vertical grid levels above the model top of the idealized simulations (400 m) are set to have a constant stretching coefficient, $\frac{z_{k+1}-z_k}{z_k-z_{k-1}}$, of 5%.

7 SIMULATION RESULTS

Our WRF-IBM simulations illustrate the complex behavior of atmospheric flows within urban environments. Figure 5, a visualization of instantaneous wind speed at 2.5 m AGL, displays channeling effects in street canyons and many other flow features including separation zones, return flows, and recirculation in the lee of buildings.

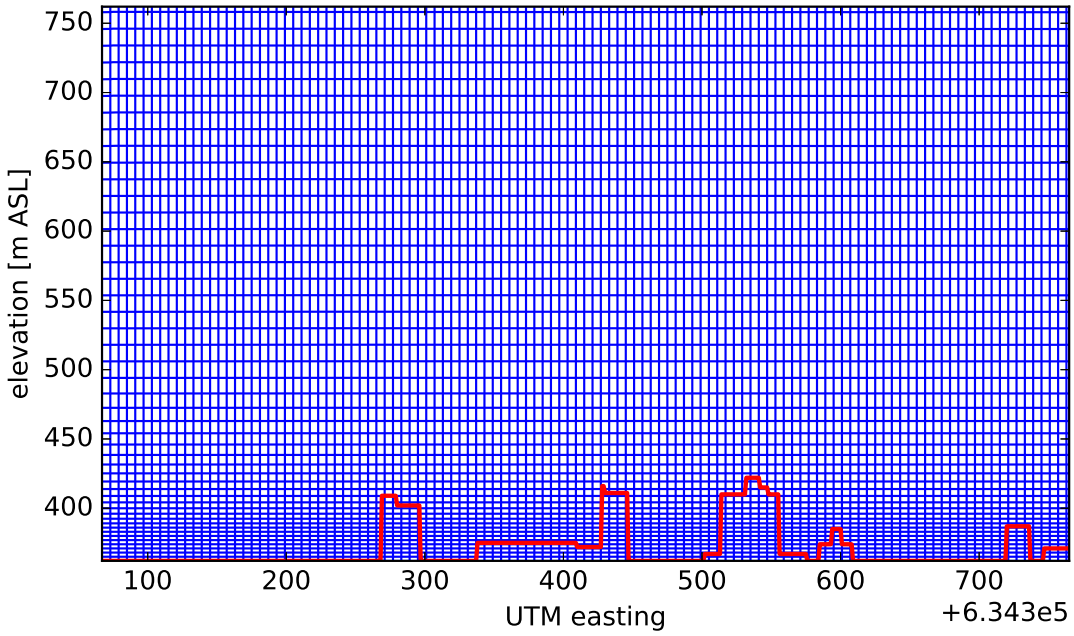

Figure 3: A west-east and vertical slice through the Oklahoma City business district from the 2 m domain of the idealized VRM simulation. Every third grid line is displayed. The immersed boundary is shown in red.

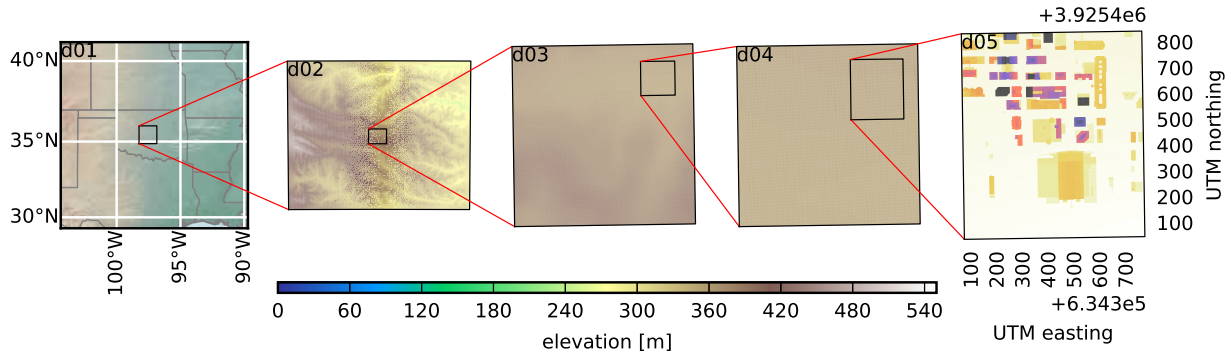

Figure 4: Configuration of domains used in the multiscale simulation centered over the business district of Oklahoma City, OK. The five domains have resolutions of 6.05 km, 550 m, 50 m, 10 m, and 2 m. The 550 m, 50 m, and 10 m domains include contour levels of topography. The 2 m domain includes contours of the building heights AGL (colorbar not shown). Dimensions of each domain and other configuration information is included in table-4

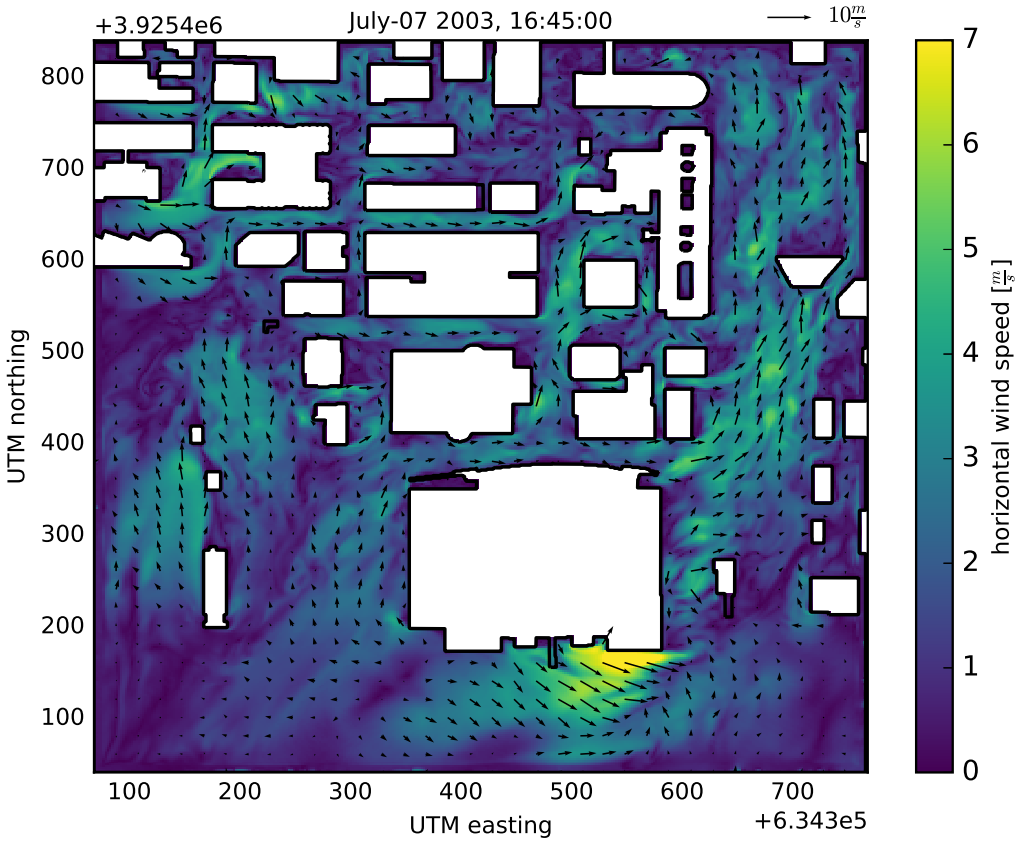

Figure 5: Instantaneous horizontal wind speed at 2.5 m AGL from the 2 m domain of the multiscale simulation at 15 minutes after the IOP 3 release start time. Quiver arrows are plotted at every tenth grid point.

During IOP 3, the ANL miniSODAR was located within the botanical gardens and sampled flow that was relatively unobstructed upstream. Compared to the miniSODAR measurements, both idealized simulations (GPM and VRM) overestimate the horizontal wind speed by up to 2.5 $\frac{m}{s}$ in the region between ground level and approximately 40 m AGL, the same height at which the pressure gradient is chosen to match the observations. The multiscale simulation, which does not include *a priori* knowledge of the observations, overestimates the velocities up to approximately 100 m AGL, as seen in Figure 6. All three simulations show excellent agreement with the measured wind direction.

One possible cause of the near surface wind speed overestimation is the omission of terrain-features upstream of the miniSODAR. In all three simulations, the 10 m domain does not include resolved buildings because most structures cannot be well represented at that resolution. An experimental setup, not shown here, with a regular array of cubes added to the terrain of the 10 m domain shows improved agreement between the 2 m domain and the observed near surface wind speed profile. If future computational resources allow, the 2 m domain could be extended southward to provide additional fetch and resolve flow around more buildings upstream from the miniSODAR and the SF_6 release location. Another potential solution could be to add artificial drag at grid points that fall within poorly resolved terrain features.

Visual comparison of model results to time-averaged wind speed/direction from DPG PWIDS (P) and super PWIDS (SP) indicate that all three simulations have similar behavior to observations within the street canyons. Some stations, such as P07, have large differences between the observed and predicted wind direction. In the case of P07, the differences are likely due to the station being located on a street corner and having close proximity to buildings. Prediction of the flow splitting at the building's sharp corner would likely be improved if the simulations were run with slightly

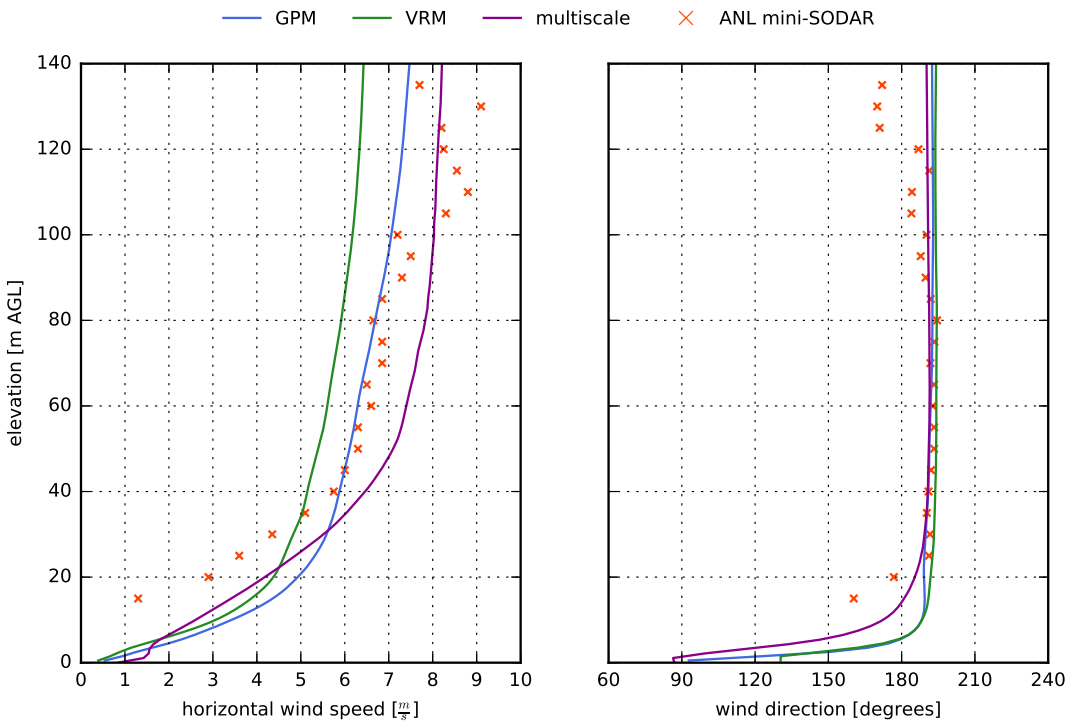

Figure 6: Vertical profiles at the ANL miniSODAR location (634451, 3925592) of horizontal wind speed and direction, time averaged over the 30 minute SF_6 release period, from the idealized VRM, idealized GPM, and multiscale simulations as well as the miniSODAR.

higher resolution and there were more grid points situated between P07 and the building corner. It should also be noted that there are often large differences measured from collocated sensors, as can be seen in Figure 7 where P08 and SP16 are located on the same measurement platform however they show a difference in time-averaged wind direction of 90 degrees.

Quantitative performance measurements of the WRF-IBM model are calculated using methods suggested by Hanna et al. (2011); fraction of predictions within a factor of x (FACx); fractional bias (FB); geometric mean bias (MG); and normalized mean squared error (NMSE). Differences in wind direction are evaluated using the scaled average angle (SAA) devised by Calhoun et al. (2004). These performance metrics have previously been applied to Joint Urban 2003 simulations by Chan and Leach (2007) and Chow et al. (2008) using the FEM3MP model, and by Lundquist et al. (2012) using the WRF-IBM-GPM model.

$$
\begin{aligned}
FACx =& \text{fraction of data that satisfies...} \\
& \ldots\ 1/x \leq X_p/X_o \leq x \\
FB =& 2\left(\overline{X_o} - \overline{X_p}\right) / \left(\overline{X_o} + \overline{X_p}\right) \\
MG =& \exp\left(\overline{\ln\left(X_o\right)} - \overline{\ln\left(X_p\right)}\right) \\
NMSE =& \overline{\left(X_o - X_p\right)^2} / \left(\overline{X_o}\ \overline{X_p}\right) \\
SAA =& \Sigma\left(|U_i||\phi_i|\right) / \left(N|\overline{U_i}|\right)
\end{aligned}
$$

In the above equations, X_o is the set of observational data and X_p are the corresponding predictions from the simulation, N is the number of observations, ϕ_i is the difference between observed and simulated wind directions, and $|U_i|$ is the simulated wind speed. Graphical representations of model skill for predicting wind speed/direction and concentration are shown in figures 8 and 9.

The idealized VRM simulation excels at predicting the magnitude and variation of wind speeds. The multiscale simulation's skill test results analyzing wind speed fall between those of the VRM and GPM simulations. GPM produced the lowest SAA, indicating that it was best at predicting wind direction. While the idealized VRM simulation matched or outperformed the

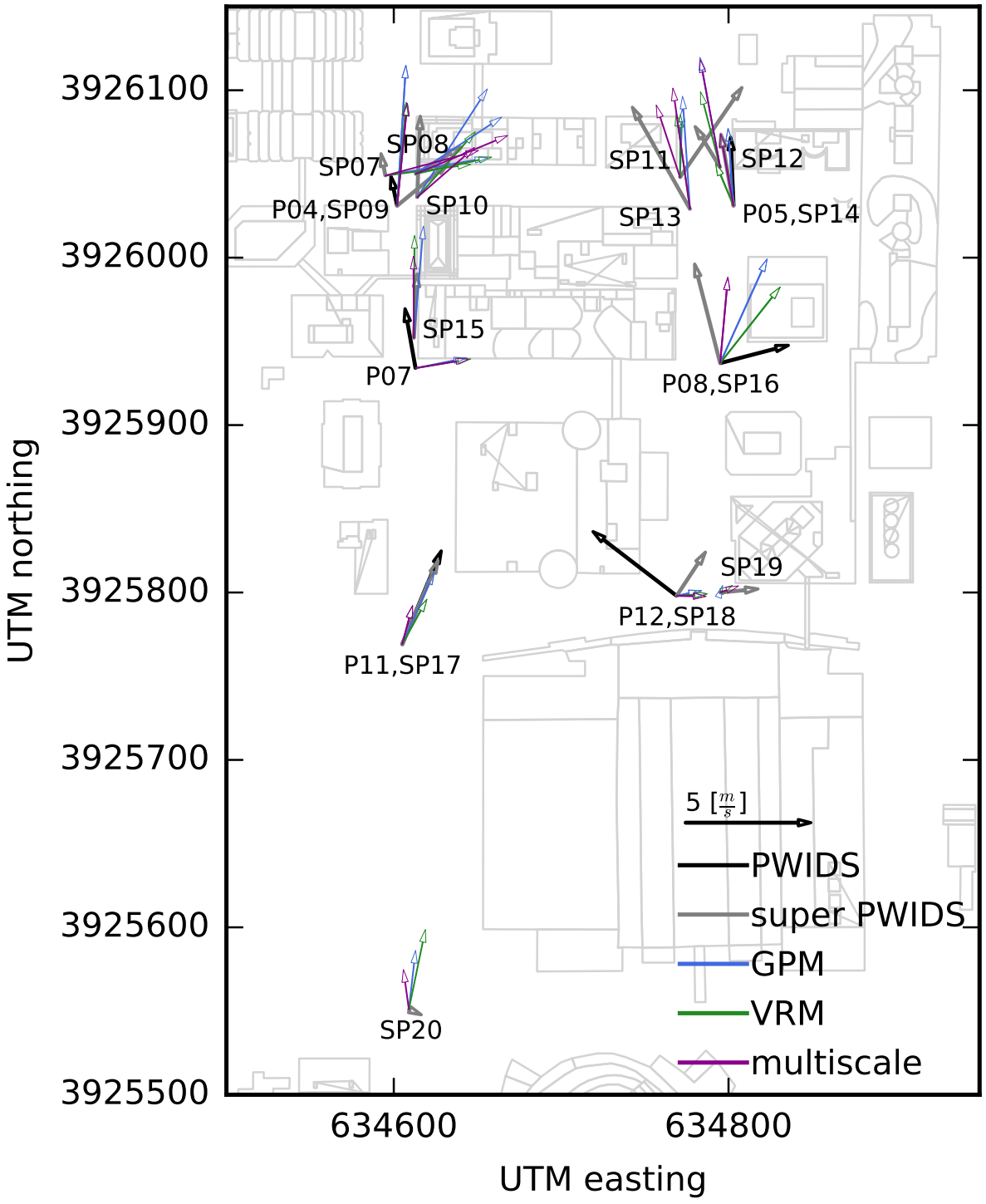

Figure 7: Horizontal wind speed and direction, time averaged over the 30 minute SF_6 release period, at the locations of DPG PWIDS (P) and DPG super PWIDS (SP). Arrows are included for observations and the three simulations (idealized GPM, idealized VRM, and multiscale).

multiscale simulation in every skill test, it is important to remember that both idealized simulations (GPM and VRM) were provided with an initialization constructed using JU2003 observations. Additionally, the forcing used for idealized simulations was tuned to maintain agreement with observations. In comparison, the multiscale simulation's initial conditions and forcing are independent of the JU2003 observations and are provided by external datasets as is typical in mesoscale forecasting. Thus, the agreement of the multiscale simulation with observations from the IOP is quite remarkable considering the absence of model tuning.

Skill tests for prediction of SF_6 concentration, Figure 9, show comparable performance between the GPM and multiscale simulations, with the VRM simulation displaying the least skill. VRM's performance could be attributed to several factors including subtle differences in wind direction at the release location, less meandering of the plume compared to the multiscale simulation, or poor agreement with elevated sensors not shown in Figure 10. The multiscale simulation skill test results show that we can achieve respectable predictions of urban dispersion by appropriately downscaling mesoscale forecasts to force microscale simulations.

8 CONCLUSIONS

Multiscale simulations over complex terrain are now possible in the WRF model through the use of vertical grid refinement and an immersed boundary method. Our simulations of a continuous tracer release from the Joint Urban 2003 field experiment show that the multiscale model initialized from a mesoscale forecast can produce simulations with model skill comparable to idealized simulations that have been initialized with local observation data.

Future model development will focus on creating improved IBM algorithms for setting scalar variables, use of a more sophisticated turbulence closure model for LES domains, and improved representation of unresolved roughness elements on intermediate grids.

Statistical tests of model skill show that the multiscale simulations initialized and forced using reanalysis data generally perform similarly with idealized simulations that have been provided appropriate initial conditions and forcing. While these initial results are promising, there are many unanswered questions about the optimal model configuration, including grid refinement ratios, turbulence seeding methods at lateral boundaries, choice of physics parameterizations, the impact of high-resolution land use and vegetation data, the importance of feedback in nested grids, and many more potential research topics.

ACKNOWLEDGEMENTS

The first author is grateful for the support of a Lawrence Scholars Program Fellowship from Lawrence Livermore National Laboratory (LLNL). This work was partially supported by the US DOE Office of Energy Efficiency and Renewable Energy (EERE) Wind Energy Technologies Office. Lawrence Livermore National Laboratory is operated by Lawrence Livermore National Security, LLC, for the U.S. Department of Energy, National Nuclear Security Administration under Contract DE-AC52-07NA27344.

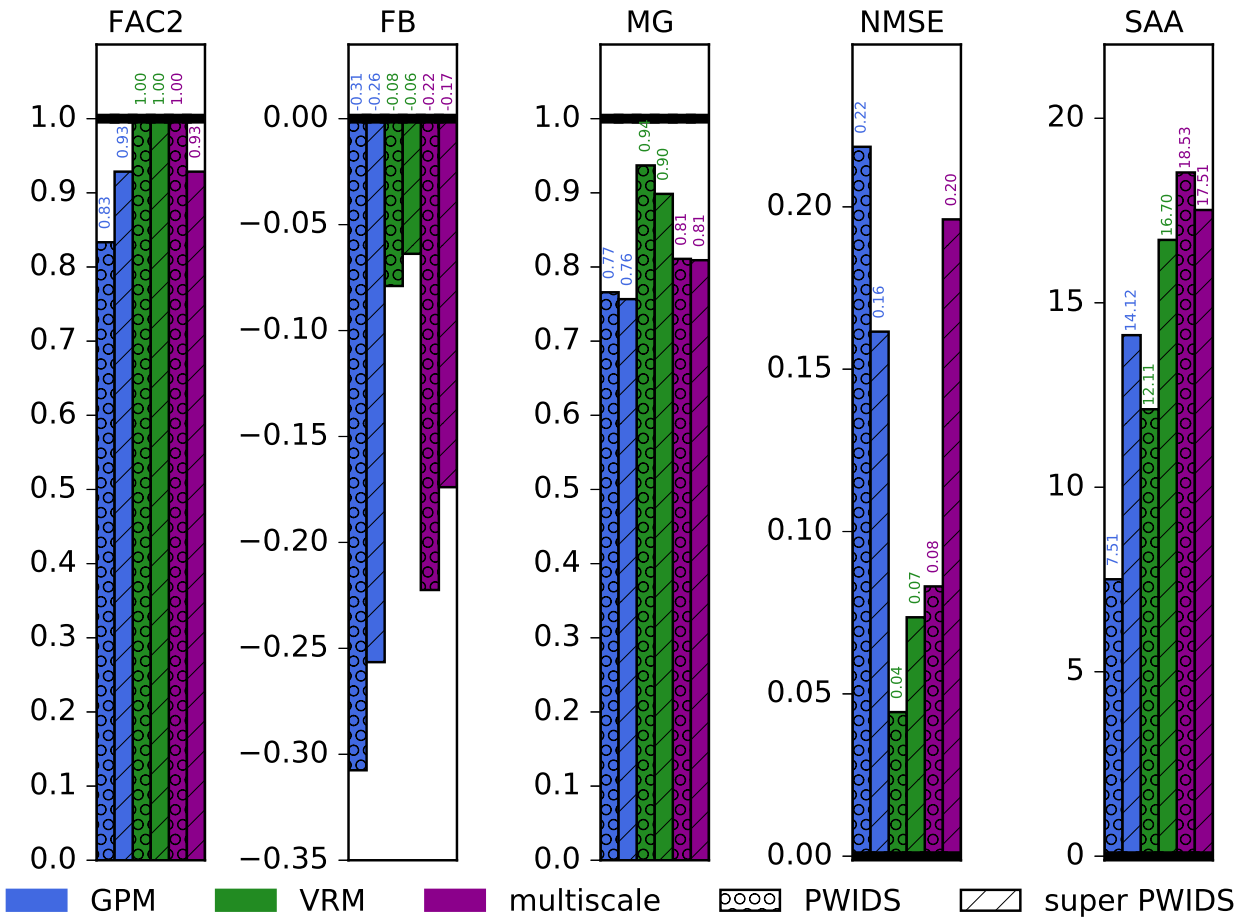

Figure 8: Model skill test results evaluating horizontal wind speed (FAC2, FB, MG, and NMSE) and wind direction (SAA) for the idealized VRM, idealized GPM, and multiscale simulations compared to the DPG PWIDS and DPG super PWIDS. The thick black lines indicate a perfect model score.

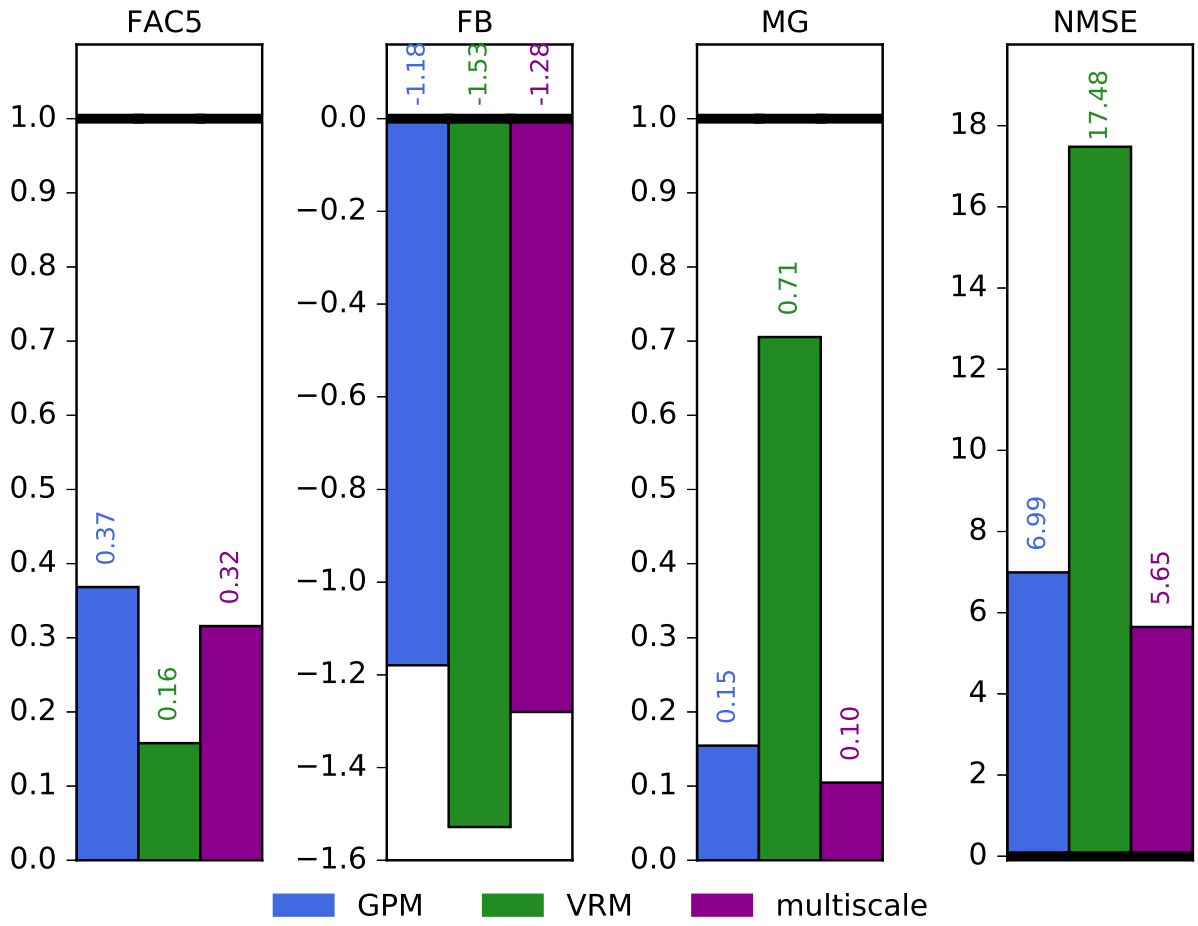

Figure 9: Model skill test results evaluating SF_6 concentration for the idealized Velocity Reconstruction Method (VRM), idealized Ghost Point Method (GPM), and multiscale simulations compared to LLNL "bluebox" integrated tracer samplers. The thick black lines indicate a perfect model score.

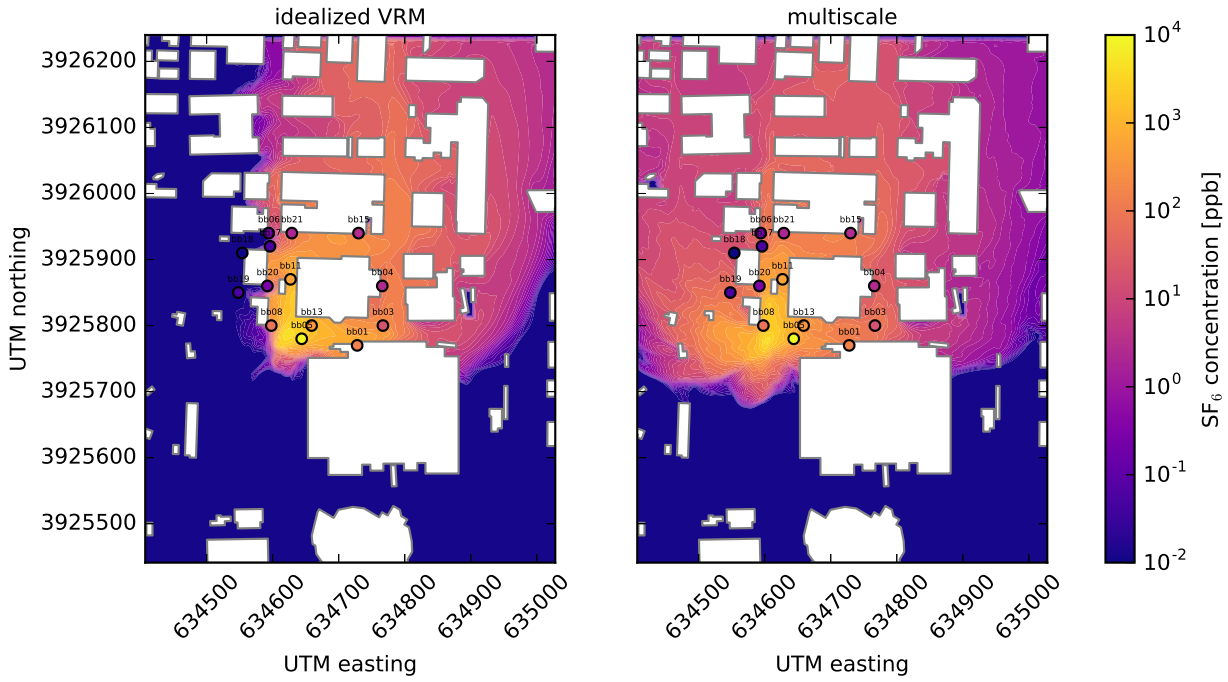

Figure 10: SF_6 concentration at 2.5 m AGL time averaged over the 30 minute release period from the idealized WRF-IBM-VRM simulation (left) and multiscale simulation (right). The circles represent time-averaged measurements from LLNL "bluebox" stations. Only stations with height of 2.5 m AGL are shown.

Appendices

station	location	UTM easting	UTM northing
P04	SW corner of Robinson/Park	634602	3926031
P05	SE corner of Broadway/Park	634803	3926031
P07	NE corner of Robinson/Main	634613	3925934
P08	NE corner of Broadway/Main	634795	3925937
P10	SW corner of Hudson/Sheridan	634319	3925766
P11	SW corner of Robinson/Sheridan	634605	3925769
P12	NW corner of Broadway/Sheridan	634769	3925798
SP07	NW corner of Robinson/Park	634595	3926049
SP08	NE corner of Robinson/Park	634613	3926050
SP09	SW corner of Robinson/Park	634602	3926031
SP10	SE corner of Robinson/Park	634614	3926036
SP11	NW corner of Broadway/Park	634771	3926048
SP12	NE corner of Broadway/Park	634795	3926054
SP13	SW corner of Broadway/Park	634777	3926029
SP14	SE corner of Broadway/Park	634803	3926031
SP15	Robinson; 75 ft. N of Robinson/Main	634612	3925952
SP16	NE corner of Broadway/Main	634795	3925937
SP17	SW corner of Robinson/Sheridan	634605	3925769
SP18	NW corner of Broadway/Sheridan	634769	3925798
SP19	NE corner of Broadway/Sheridan	634795	3925800
SP20	NW corner of Robinson/Reno	634609	3925551

Table 1: Siting information for Dugway Proving Grounds Portable Weather Information Display Systems (P) with prop-vane anemometers and super PWIDS (SP) with sonic anemometers.

station	location	UTM easting	UTM northing	height AGL
bb01	Convention Center, Ground Level	634728	3925770	1
bb03	Sheridan and Broadway, NW	634767	3925800	1
bb04	Westin Lobby, Ground Level	634766	3925860	1
bb05	Robinson and Sheridan, SE	634644	3925780	1
bb06	Robinson and Main, NW	634594	3925940	1
bb08	Robinson and Sheridan Ground, NW	634598	3925800	1
bb09	Robinson and Sheridan Roof, NW	634598	3925800	40
bb11	Century Center, West, Ground	634627	3925870	1
bb12	Century Center, West, Roof	634627	3925870	18
bb13	Century Center, South, Ground	634659	3925800	1
bb14	Century Center, South, Roof	634659	3925800	18
bb15	Main Street Parking, Ground	634730	3925940	1
bb16	Main Street Parking, Roof	634730	3925940	26
bb17	Robinson Plaza, NE	634596	3925920	1
bb18	Robinson Plaza, NW	634554	3925910	1
bb19	Robinson Plaza, SW	634548	3925850	1
bb20	Robinson Plaza, SE	634592	3925860	1
bb21	Robinson and Main, NE	634629	3925940	1
bb22	OKLand Bldg., Roof	634629	3925940	18

Table 2: LLNL blue box integrated tracer sampler siting information in Universal Transverse Mercator coordinates.

height AGL [m]	U $[\frac{m}{s}]$	V $[\frac{m}{s}]$
2.0	0.9165	-0.0802
8.0	1.1521	1.9408
15.0	-0.3909	1.2398
20.0	-0.0253	2.8999
25.0	1.0525	3.4427
30.0	1.2355	4.1709
35.0	1.2769	4.9376
40.0	1.4882	5.5541
45.0	1.5529	5.7956
50.0	1.7365	6.0559
55.0	1.7893	6.0406
60.0	1.6525	6.3898
65.0	1.7370	6.2636
70.0	1.6572	6.6465
75.0	1.8881	6.5846
80.0	2.0550	6.3245
85.0	1.8306	6.6009
90.0	1.7042	7.0983
95.0	1.6233	7.3222
100.0	1.9846	6.9211
105.0	0.7234	8.2684
110.0	1.0725	8.7344
115.0	1.7046	8.3784
120.0	1.0054	8.1885
125.0	-1.2828	8.0990
130.0	-1.5802	8.9618
135.0	-1.0716	7.6251
150.0	-1.0716	7.6251
400.0	-1.0716	7.6251

Table 3: Vertical profile of U and V velocities used for the WRF-IBM model initialization. This is generated by combining data from the ANL miniSODAR with nearby DPG PWIDS (P10 and P11) and DPG super PWIDS (SP17 and SP20).

	D1	D2	D3	D4	D5
Δx & Δy [m]	6050	550	50	10	2
coordinate	TF	TF	TF	IBM	IBM
time-step [s]	30	3	0.25	0.05	0.01
east-west grid points	221	232	254	241	351
south-north grid points	221	232	254	241	401
bottom-top grid points	51	51	76	146	243
turbulence	MYJ	MYJ	Smag	Smag	Smag
micro-physics	WSM3	WSM3	WSM3	none	none
longwave radiation	RRTM	RRTM	RRTM	RRTM	none
shortwave radiation	Dudhia	Dudhia	Dudhia	Dudhia	none
surface layer scheme	MM5	MM5	MM5	MM5	none
land surface model	Noah	Noah	Noah	Noah	none
cumulus parameterization	KF	KF	none	none	none

Table 4: Multiscale model configuration for JU2003 simulations. TF = terrain-following coordinate. KF = Kain-Fritsch cumulus parameterization.

References

Allwine, J., and J. Flaherty, 2006: Joint Urban 2003: Study overview and instrument locations. Tech. Rep. PNNL-15967, Pacific Northwest National Laboratory. [Available online at https://pnnl.gov/main/publications/external/technical_reports/PNNL-15967.pdf].

Arthur, R., K. Lundquist, J. Mirocha, and F. K. Chow, 2018: Topographic effects on radiation in the wrf model with the immersed boundary method: implementation, validation, and application to complex terrain. *Monthly Weather Review*, in revision.

Arthur, R., K. Lundquist, J. Mirocha, S. Hoch, and F. K. Chow, 2016: High-resolution simulations of downslope flows over complex terrain using wrf-ibm. *17th Conference on Mountain Meteorology*, Burlington, VT, American Meteorological Society.

Bao, J., K. Lundquist, and F. K. Chow, 2016: Comparison of different implementations of the immersed boundary method in WRF. *22th Symposium on Boundary Layers and Turbulence*, Salt Lake City, UT, American Meteorological Society.

Bao, J., K. Lundquist, and F. K. Chow, 2018: Large-eddy simulation over complex terrain using an improved immersed boundary method in the Weather Research and Forecasting model. *Monthly Weather Review*, in press.

Calhoun, R., F. Gouveia, J. Shinn, S. Chan, D. Stevens, R. Lee, and J. Leone, 2004: Flow around a complex building: Comparisons between experiments and a reynolds-averaged navier-stokes approach. *Journal of Applied Meteorology*, **43**, 696–710, doi:10.1175/2067.1.

Chan, S., and M. Leach, 2007: A validation of FEM3MP with Joint Urban 2003 data. *Journal of Applied Meteorology and Climatology*, **46**, 2127–2146, doi:10.1175/2006JAMC1321.1.

Chow, F. K., B. Kosović, and S. Chan, 2008: Source inversion for contaminant plume dispersion in urban environments using building-resolving simulations. *Journal of Applied Meteorology and Climatology*, **47**, 1553–1572, doi:10.1175/2007JAMC1733.1.

Daniels, M., K. Lundquist, J. Mirocha, D. Wiersema, and F. K. Chow, 2016: A new vertical grid nesting capability in the weather research and forecasting (WRF) model. *Monthly Weather Review*, **144 (10)**, 3725–3747, doi:10.1175/MWR-D-16-0049.1.

Hanna, S., and Coauthors, 2011: Comparisons of JU2003 observations with four diagnostic urban wind flow and Lagrangian particle dispersion models. *Atmospheric Environment*, **45**, 4073–4081.

Lundquist, K., 2010: Immersed boundary methods for high-resolution simulation of atmospheric boundary-layer flow over complex terrain. Ph.D. thesis, Univeristy of California, Berkeley.

Lundquist, K., F. K. Chow, and J. Lundquist, 2010: An immersed boundary method for the weather research and forecasting model. *Monthly Weather Review*, **138**, 796–817.

Lundquist, K., F. K. Chow, and J. Lundquist, 2012: An immersed boundary method enabling large-eddy simulations of complex terrain in the wrf model. *Monthly Weather Review*, **140 (12)**, 3936–3955, doi:10.1175/MWR-D-11-00311.1.

Mesinger, F., and Coauthors, 2006: North american regional reanalysis: A long-term, consistent, high-resolution climate dataset for the north american domain, as a major improvement upon the earlier global reanalysis datasets in both resolution and accuracy. *Bulletin of the American Meteorological Society*, **87**, 342–360, doi:10.1175/BAMS-87-3-343.

Mirocha, J., G. Kirkil, E. Bou-Zeid, F. K. Chow, and B. Kosović, 2013: Transition and equilibrium of neutral atmospheric boundary layer flow in one-way nested large-eddy simulations using the weather research and forecasting model. *Monthly Weather Review*, **141**, 918–940, doi:10.1175/MWR-D-11-00263.1.

Neophytou, M., A. Gowardhan, and M. Brown, 2011: An inter-comparison of three urban wind models using Oklahoma City Joint Urban 2003 wind field measurements. *Journal of Wind Engineering and Industrial Aerodynamics*, **99**, 357–368, doi:10.1016/j.jweia.2011.01.010.

Peskin, C. S., 1972: Flow patterns around heart valves: A digital computer method for solving the equations of motion. Ph.D. thesis, Albert Einstein College of Medicine, [Available from: http://www.umi.com/hp/Products/DisExpress.html, order no. 7230378].